Title

Directly detected 55Mn MRI: Application to phantoms for human hyperpolarized 13C MRI development

Journal

Magnetic Resonance Imaging, 32(10)

ISSN

0730-725X

Authors

von Morze, Cornelius

Carvajal, Lucas

Reed, Galen D

et al.

Publication Date

2014-12-01

DOI

10.1016/j.mri.2014.08.030

Peer reviewed

Published in final edited form as:
Magn Reson Imaging. 2014 December ; 32(10): 1165–1170. doi:10.1016/j.mri.2014.08.030.

Directly detected ^{55}Mn MRI: Application to phantoms for human hyperpolarized ^{13}C MRI development

Cornelius von Morze, Ph.D.[1], **Lucas Carvajal, M.S.**[1], **Galen D. Reed, B.S.**[1,2], **Christine Leon Swisher, M.S.**[1,2], **James Tropp, Ph.D.**[3], and **Daniel B. Vigneron, Ph.D.**[1,2]

[1] Department of Radiology and Biomedical Imaging, University of California, San Francisco

[2] UC Berkeley-UCSF Graduate Program in Bioengineering, University of California, San Francisco and University of California, Berkeley

[3] GE Healthcare, Fremont, California

Abstract

In this work we demonstrate for the first time directly detected manganese-55 (^{55}Mn) MRI using a clinical 3T MRI scanner designed for human hyperpolarized ^{13}C clinical studies with no additional hardware modifications. Due to the similar frequency of the ^{55}Mn and ^{13}C resonances, the use of aqueous permanganate for large, signal-dense, and cost-effective "^{13}C" MRI phantoms was investigated, addressing the clear need for new phantoms for these studies. Due to 100% natural abundance, higher intrinsic sensitivity, and favorable relaxation properties, ^{55}Mn MRI of aqueous permanganate demonstrates dramatically increased sensitivity over typical ^{13}C phantom MRI, at greatly reduced cost as compared with large ^{13}C-enriched phantoms. A large sensitivity advantage (22-fold) was demonstrated. A cylindrical phantom (d= 8 cm) containing concentrated aqueous sodium permanganate (2.7M) was scanned rapidly by ^{55}Mn MRI in a human head coil tuned for ^{13}C, using a balanced SSFP acquisition. The requisite penetration of RF magnetic fields into concentrated permanganate was investigated by experiments and high frequency electromagnetic simulations, and found to be sufficient for ^{55}Mn MRI with reasonably sized phantoms. A sub-second slice-selective acquisition yielded mean image SNR of ~60 at 0.5cm^3 spatial resolution, distributed with minimum central signal ~40% of the maximum edge signal. We anticipate that permanganate phantoms will be very useful for testing HP ^{13}C coils and methods designed for human studies.

Introduction

Manganese-55 (^{55}Mn) is a spin-5/2 nucleus with 100% natural abundance, high intrinsic NMR sensitivity, and gyromagnetic ratio very close to ^{13}C (γ_{55Mn}= 10.56 MHz / T , γ_{13C}=

Corresponding author: Cornelius von Morze, Department of Radiology and Biomedical Imaging, University of California, San Francisco, 1700 Fourth Street, Byers Hall Suite 102, San Francisco, CA 94158, cornelius.vonmorze@ucsf.edu Phone: 415-514-4455, Fax: 415-514-4451.

10.70 MHz / T) [1, 2]. Paramagnetic forms of ^{55}Mn are well known modifiers of ^{1}H relaxivity, including the FDA-approved hepatobiliary MRI contrast agent mangafodipir trisodium (MnDPDP) [3, 4], but to our knowledge there has been no prior study of directly detected ^{55}Mn MRI. In contrast to its other common oxidation states, the +7 state is only very weakly paramagnetic and yields a sensitive NMR signal for aqueous solutions of the permanganate ion [5]. In this study we report the first ever directly detected ^{55}Mn MRI images, acquired rapidly using a customized clinical 3T MRI scanner designed for human hyperpolarized (HP) ^{13}C studies, with no additional hardware modifications required for ^{55}Mn MRI. At 3T, the frequency offset of ~450 kHz for ^{55}Mn relative to ^{13}C is well within the operable bandwidth of a clinical MRI scanner equipped with multinuclear ^{13}C capability.

Due to the high proximity of the ^{55}Mn resonance to ^{13}C, a logical application of ^{55}Mn MRI is for large, signal-dense, and cost-effective "^{13}C" phantoms, which are needed to help investigate new methods designed for HP ^{13}C imaging of humans based on dissolution DNP [6], and to perform tests of new clinical ^{13}C coils and related hardware. The clinical translational potential of HP ^{13}C MRI [7, 8] is motivating the development of specially designed novel MRI techniques, which will be critical to the realization of the full potential of this exciting new technology. Areas of research include the development of efficient, highly accelerated MRI pulse sequences and their associated reconstruction methods [9-13], methods for flip angle mapping to enable precisely controlled expenditure of the non-renewable magnetization [14, 15], and the design and construction of optimized ^{13}C RF coils and coil arrays for maximum coverage and speed [16-19]. However, the low natural abundance of ^{13}C (1%) limits the concentration of non-enriched phantom solutions to ~400 mM NMR active nuclei, resulting in poor sensitivity. The large-scale enrichment needed to produce large ^{13}C imaging phantoms with sensitivity at least remotely comparable to HP imaging conditions is cost-prohibitive. For example, the cost of enriching a single 4L human head phantom to 4M ^{13}C (e.g. requiring 1kg [^{13}C]urea, one of the least expensive, highly soluble, ^{13}C-enriched substances available) is tens of thousands of dollars, even assuming a sizable discount over currently advertised prices for smaller quantities. Producing HP material simply for phantom experiments is tedious and also costly, especially for large volumes, and testing procedures are limited by T_1 relaxation. The limitations of practical carbon phantoms thus are restricting the ability to develop and test new methods for HP ^{13}C imaging, particularly as research moves from the preclinical scale to the larger human scale.

Due to 100% natural abundance of ^{55}Mn, a relatively inexpensive solution of aqueous permanganate can provide NMR-active nuclear concentrations in the molar range at a Larmor frequency very close to ^{13}C, with an added sensitivity boost of about one order of magnitude over ^{13}C due to higher intrinsic NMR sensitivity of the spin-5/2 ^{55}Mn nucleus. Favorable relaxation properties of permanganate solutions further contribute to high sensitivity of ^{55}Mn MRI ($T_1 \approx T_2$), by facilitating continuously large transverse magnetizations. Potassium permanganate ($KMnO_4$), the most common salt, is a widely used oxidant, applied in water treatment procedures and various organic syntheses. The less common sodium salt ($NaMnO_4$) has similar chemical properties but is much more water-soluble. The estimated sensitivity advantage of using concentrated aqueous $NaMnO_4$ (e.g. 3.0M) as a source of "^{13}C" phantom signal is at least two orders of magnitude over the best

natural abundance carbon solutions (e.g. ethylene glycol, 360mM ^{13}C), bringing the sensitivity of thermal phantom experiments much closer to the HP regime. At 3T, 3.0M $NaMnO_4$ has theoretically roughly equivalent sensitivity to 3.0mM HP ^{13}C with 10,000-fold enhancement over the thermal level (i.e. 2.7% polarization), which is comparable to typical experimental HP conditions after dilution *in vivo*.

In this study we investigated rapid ^{55}Mn MRI of a concentrated aqueous permanganate phantom within a clinical 3T MRI system designed for ^{13}C imaging, with a focus on simulating the high sensitivity of HP ^{13}C studies. We tested the phantom's utility for replicating the high sensitivity of *in vivo* HP ^{13}C conditions, as compared to a standard natural abundance ethylene glycol phantom. We also applied high frequency electromagnetic analysis to evaluate the requisite penetration of resonant RF magnetic fields for ^{55}Mn and ^{1}H into aqueous $NaMnO_4$ solution at 3T, which is potentially hindered by the relatively high electrical conductivity of ionic solutions at high concentrations such as in this phantom, producing potentially significant "skin effects" even at low frequencies.

Methods

Phantoms

MRI phantoms consisted of two cylindrical glass bottles of identical size and shape, with inner diameter 8 cm (Wheaton, Millville, NJ). Each bottle had a uniform cylindrical cross-section of 12 cm in length, which then tapered over 3 cm to a screw-capped opening of diameter 2 cm. Ethylene glycol and aqueous $NaMnO_4$ (40% wt/wt or 3.9M) were obtained commercially (Sigma, St. Louis, MO). The aqueous $NaMnO_4$ was diluted to 2.7M with distilled water. Phantoms were filled to the brim with 650 mL natural abundance ethylene glycol or aqueous $NaMnO_4$ (2.7M). Bottles were clear in the case of ethylene glycol and opaque for aqueous $NaMnO_4$ in order to minimize photodecomposition.

MRI hardware

The MRI scanner was a 3T clinical imaging system equipped with multinuclear ^{13}C capability (GE Healthcare, Waukesha, WI). The RF coil used to image ^{55}Mn was a custom 26-cm cylindrical birdcage transceiver coil tuned for ^{13}C and designed for imaging a human head. The bench-derived RF coil match at the ^{55}Mn frequency (31.7 MHz) with loading was $|S_{11}| \approx -5$ dB on both quadrature channels, as compared with −20 dB at the ^{13}C frequency (32.1 MHz). The coil was connected to the standard system-embedded amplifiers for ^{13}C MRI. The body RF coil was used to obtain ^{1}H images. Since this ^{13}C coil lacked ^{1}H trap circuits to block ^{1}H RF transmit power, it was slid out of its holder for ^{1}H imaging, without moving the phantoms.

MRI experiments

The T_1 and T_2 relaxation times of aqueous $NaMnO_4$ were measured at 3T. T_1 was measured by least squares fitting of non-localized FID data from a saturation recovery scheme using a 1ms hard pulse followed immediately by readout, with varying repetition times (TR= 50ms, 75ms, 100ms, 125ms, 150ms). T_2 was measured by fitting non-localized FID data from a Carr Purcell Meiboom Gill (CPMG) pulse train (32 echoes, TE_1= 10.3ms, echo spacing=

20.6ms). For comparison, a 90° "pulse and acquire" FID with identical pulse length and readout was acquired for both the $NaMnO_4$ phantom and the identical ethylene glycol phantom, with recalibration of the transmit gain for each nucleus. For this experiment, the ethylene glycol was substituted for the $NaMnO_4$ phantom in the same spatial position, close to the center of the RF coil. Axial RF spoiled gradient echo (SPGR) ^{1}H 2D multi-slice images were acquired (matrix= 128×128, FOV= 16 cm, slice thickness= 10 mm, number of slices= 8, TE / TR = 10 ms / 2 s, $BW_{frequency}$= ±10 kHz). Rapid axial slice selective ^{55}Mn MRI of the $NaMnO_4$ phantom was performed using a custom balanced steady state free precession (bSSFP) multi-slice pulse sequence acquired at both a lower spatial resolution (5×5mm^2 in-plane, matrix= 32×24, FOV= 16cm×12cm, slice thickness= 20 mm, slice gap= 20 mm, N_{slices}=4, α= 60°, TE / TR= 6ms / 12ms, $BW_{frequency}$= ±10 kHz, RF excitation= 3.2 ms sinc pulse, scan time= 300 ms per image or 1.2 s total) and a higher spatial resolution (2.5×2.5mm^2 in-plane, matrix= 64×48, $N_{averages}$= 12, scan time= 6.9 s per image or 27.6 s total, all other parameters identical to low resolution acquisition). Based on Bloch simulations, the bSSFP scheme facilitated rapid formation of a signal steady state based on transverse magnetization of magnitude equal to roughly half the longitudinal magnetization at thermal equilibrium.

Electromagnetic simulations

We analyzed the penetration of RF magnetic fields into simulated cylindrical aqueous $NaMnO_4$ phantoms for both ^{55}Mn and ^{1}H MRI. The complex magnetic vector potential field $\vec{A}$ for a lossy dielectric cylinder of diameter *d* and infinite length along $\hat{z}$, with RF conductivity σ and permittivity $\varepsilon\varepsilon_0$, excited by a uniform external RF magnetic field with linear polarization along $\hat{x}$, has analytic solution [20, 21]

$$\vec{A}\,(r,\phi) = -2B_{1,0}\frac{J_1\,(kr)\,sin\phi}{kJ_0\,(kd/2)}\hat{z}$$

where *r* and ϕ are standard polar coordinates with origin defined at the center of the cylinder, $B_{1,0}$ is the magnetic field amplitude prior to its introduction, J_0 and J_1 are Bessel functions of order 0 and 1 respectively, and *k* is the complex wavenumber given by $k^2 = j\omega\mu_0\sigma + \omega\varepsilon\varepsilon_0\mu_0$. The vector potential for the case of external circular polarization was obtained by superposition of an additional identical term oriented in spatiotemporal quadrature with the first. The corresponding complex transverse magnetic field $\vec{B}$, which is in general elliptically polarized, was obtained by numerically computing $\vec{\nabla} \times \vec{A}$.

MRI images are modulated by "antenna patterns" for transmission and reception that can be derived from the transmit RF "field pattern" as defined above [22]. MRI image intensity *S* at a given spatial position is proportional to the product of these two patterns

$$S \propto |B_x + jB_y||(B_x + jB_y)^*|$$

where * denotes the operation of complex conjugation. The product of these two antenna patterns was computed over space for each simulated phantom.

The simulation parameters were: $\varepsilon = 78$, $d = 8$ cm, $\omega_{55Mn} = 2\pi 3.17 MHz$, $\omega_{1H} = 2\pi 127.7 MHz$ and $\sigma = 23.5$ *S/m*. This estimated conductivity is much higher than typical physiologic values relevant to MRI (~0.5 S/m). The RF conductivity of aqueous $NaMnO_4$ was assumed to be linear with concentration (2.7M), with coefficient 8.7 S/m per molar $NaMnO_4$ derived from prior work on DC electrical resistivity imaging of concentrated aqueous $NaMnO_4$ groundwater injections, conducted for the purpose of monitoring groundwater remediation procedures [23].

Results

The monoexponential ^{55}Mn NMR T_1 and T_2 relaxation times of aqueous $NaMnO_4$ at 3T were measured to be 82 ms (goodness of fit parameter $R^2 = 0.95$) and 67 ms ($R^2 = 0.99$), respectively. For the two phantoms of identical size and shape, the transmit gain required to achieve a 90° pulse for ^{55}Mn NMR of the $NaMnO_4$ phantom was 9.0 dB higher than for ^{13}C NMR of the ethylene glycol phantom. The 90° “pulse and acquire” spectral SNR was 22x higher for ^{55}Mn NMR of $NaMnO_4$ as compared with ^{13}C NMR of natural abundance ethylene glycol. Comparative spectra are shown in Figure 1.

Rapid ^{55}Mn bSSFP MRI images of the aqueous $NaMnO_4$ phantom were formed, with approximate mean SNR of 60:1 for the $5\times5 mm^2$ (32×24) resolution acquisition (300 ms per image), and 37:1 for the $2.5\times2.5 mm^2$ (64×48) resolution acquisition (6.9s per image). Phantom images acquired at both resolutions are given in Figure 2.

Despite the application of birdcage resonators for both ^{1}H MRI (body coil) and ^{55}Mn MRI (insert head coil), which ideally produce highly uniform antenna patterns for transmit and receive at low frequency, both the ^{1}H and ^{55}Mn images exhibited significant image intensity artifacts, evidencing departure from the quasi-static regime. Artifacts were moderate in the case of ^{55}Mn MRI and severe in the case of ^{1}H MRI. In particular, classic electromagnetic “skin effects” were observed, where a conductive sample tends to exclude high frequency magnetic fields from its interior. The approximate appearance of these artifacts at both frequencies was replicated in the electromagnetic simulations (Figure 3). The ^{55}Mn images exhibited an additional shading artifact associated with quadrature imbalance of the birdcage coil, whose general appearance was also replicated in simulations by scaling one of the two linear modes of the external transmit field (Figure 4).

Discussion

The results demonstrate the feasibility of high sensitivity ^{55}Mn MRI using hardware designed for human HP ^{13}C studies for testing new sequence and coil methodologies addressing the prohibitively high-cost of producing large ^{13}C-enriched phantoms. The experimental results demonstrated a 22-fold sensitivity advantage over natural abundance ethylene glycol and showed that RF penetration into concentrated aqueous $NaMnO_4$ samples is sufficient for ^{55}Mn MRI of phantoms of at least 8 cm in diameter. They also demonstrated the feasibility of ^{13}C SSFP imaging at the human scale, which will be required to exploit the recently recognized long T_2’s of ^{13}C nuclei of interest for human applications such as [1-^{13}C]pyruvate and [^{13}C,$^{15}N_2$]urea [24, 25].

The magnitude of associated artifacts was somewhat less than predicted by simulations, especially for ^{55}Mn MRI. This may result from overestimation of the true RF conductivity of the phantom, which may be frequency dependent and non-linear at high concentration, and/or lowering of the RF permittivity of water by the addition of $NaMnO_4$. Both of these parameters are difficult to measure. Potential methods for reducing the remaining RF penetration artifacts include refrigeration of the $NaMnO_4$ phantom, or dilution, which would result in a trade-off of sensitivity vs. artifact level. The chosen concentration of 2.7M may not necessarily be optimal. The optimal concentration could depend on the coil, phantom diameter, field strength, etc. In this case, a modest dilution to the range of 1-2M would be reasonable. It is important to point out that the same RF penetration considerations would also apply to large, concentrated ^{13}C-enriched phantoms containing ionic solutions, which represent some of the most reasonable options for producing large phantoms (e.g. sodium acetate). Since spectrally selective metabolic imaging is a major focus of HP ^{13}C studies, a useful further development of this work would be the design of permanganate phantoms with multiple distinct spectral lines. A possible implementation would be the construction of a phantom with separate compartments containing permanganate in different solvents (e.g. H_2O and D_2O).

Permanganates like many phantom solutions require some special handling due to potential reactivity and toxicities but this did not limit its use or applicability for these studies. Although stable in appropriate enclosed containers such as glass bottles, permanganates are potent oxidants and are therefore incompatible with some materials. For example, mixture with ethylene glycol can result in combustion and is therefore excluded. Although small levels of manganese are critical for biologic function, human exposure to supra-physiologic levels of manganese is potentially dangerous. Phantoms and their handling procedures need be designed to prevent skin or mucosal contact with the solution, and gloves should be worn when handling the material as small quantities may stain the skin. These precautions were easily accomplished in this project.

Considering the high sensitivity observed, we speculate that ^{55}Mn MRI could have *ex vivo* industrial value. Also, if chemically stabilized versions of permanganate could be formulated, which could shield tissue from its high redox potential and potential toxicities, ^{55}Mn MRI could itself be an interesting *in vivo* modality for direct, background-free molecular imaging. One could envision a chemically bound formulation of permanganate that renders sufficient quantities safe for use *in vivo*, similar to Gd chelates. Analogous chemical stabilization procedures have previously been applied to permanganate to meet other objectives including slow-release characteristics or modified specificity for oxidation targets, for example by encapsulation into a polymer matrix or adsorption onto silica gels, respectively [26, 27].

Acknowledgments

This study was supported in part by NIH grants P41EB013598, R01EB013427, R01EB017449, R01CA183071 and K01DK099451.

References

[1]. Proctor WG, Yu FC. On the Nuclear Magnetic Moments of Several Stable Isotopes. Physical review. 1951; 81(1):20–30.

[2]. Lutz O, Steinkil W. 55manganese Nuclear Magnetic Resonance Studies. Phys Lett A. 1969; A 30(3):183.

[3]. Koretsky AP, Silva AC. Manganese-enhanced magnetic resonance imaging (MEMRI). Nmr Biomed. Dec; 2004 17(8):527–31. [PubMed: 15617051]

[4]. Federle M, Chezmar J, Rubin DL, Weinreb J, Freeny P, Schmiedl UP, et al. Efficacy and safety of mangafodipir trisodium (MnDPDP) injection for hepatic MRI in adults: results of the U.S. Multicenter phase III clinical trials. Efficacy of early imaging. Journal of magnetic resonance imaging : JMRI. Nov; 2000 12(5):689–701. [PubMed: 11050638]

[5]. Gudlin D, Schneider H. Manganese-55 Nuclear Magnetic-Resonance Studies of Potassium Permanganate Solutions at 22 Degreesc. Journal of Magnetic Resonance. 1975; 17(2):268–71.

[6]. Ardenkjaer-Larsen JH, Fridlund B, Gram A, Hansson G, Hansson L, Lerche MH, et al. Increase in signal-to-noise ratio of > 10,000 times in liquid-state NMR. Proc Natl Acad Sci USA. Sep 2; 2003 100(18):10158–63. [PubMed: 12930897]

[7]. Malloy CR, Merritt ME, Sherry AD. Could 13C MRI assist clinical decision-making for patients with heart disease? Nmr Biomed. Oct; 2011 24(8):973–9. [PubMed: 21608058]

[8]. Kurhanewicz J, Vigneron DB, Brindle K, Chekmenev EY, Comment A, Cunningham CH, et al. Analysis of cancer metabolism by imaging hyperpolarized nuclei: prospects for translation to clinical research. Neoplasia. Feb; 2011 13(2):81–97. [PubMed: 21403835]

[9]. Hu S, Lustig M, Balakrishnan A, Larson PE, Bok R, Kurhanewicz J, et al. 3D compressed sensing for highly accelerated hyperpolarized (13)C MRSI with in vivo applications to transgenic mouse models of cancer. Magnetic resonance in medicine : official journal of the Society of Magnetic Resonance in Medicine / Society of Magnetic Resonance in Medicine. Feb; 2010 63(2):312–21.

[10]. Larson PE, Hu S, Lustig M, Kerr AB, Nelson SJ, Kurhanewicz J, et al. Fast dynamic 3D MR spectroscopic imaging with compressed sensing and multiband excitation pulses for hyperpolarized 13C studies. Magnetic resonance in medicine : official journal of the Society of Magnetic Resonance in Medicine / Society of Magnetic Resonance in Medicine. Mar; 2011 65(3):610–9.

[11]. Lau AZ, Chen AP, Hurd RE, Cunningham CH. Spectral-spatial excitation for rapid imaging of DNP compounds. Nmr Biomed. Oct; 2011 24(8):988–96. [PubMed: 21751271]

[12]. Mayer D, Levin YS, Hurd RE, Glover GH, Spielman DM. Fast metabolic imaging of systems with sparse spectra: application for hyperpolarized 13C imaging. Magn Reson Med. Oct; 2006 56(4):932–7. [PubMed: 16941617]

[13]. Reed GD, Larson PE, Morze C, Bok R, Lustig M, Kerr AB, et al. A method for simultaneous echo planar imaging of hyperpolarized (13)C pyruvate and (13)C lactate. Journal of magnetic resonance. Apr.2012 217:41–7. [PubMed: 22405760]

[14]. Lau AZ, Chen AP, Cunningham CH. Integrated Bloch-Siegert B(1) mapping and multislice imaging of hyperpolarized (1)(3)C pyruvate and bicarbonate in the heart. Magnetic resonance in medicine : official journal of the Society of Magnetic Resonance in Medicine / Society of Magnetic Resonance in Medicine. Jan; 2012 67(1):62–71.

[15]. Puckeridge M, Pages G, Kuchel PW. Simultaneous estimation of T(1) and the flip angle in hyperpolarized NMR experiments using acquisition at non-regular time intervals. Journal of magnetic resonance. Sep.2012 222:68–73. [PubMed: 22820261]

[16]. Dominguez-Viqueira W, Lau AZ, Chen AP, Cunningham CH. Multichannel receiver coils for improved coverage in cardiac metabolic imaging using prepolarized (13) C substrates. Magnetic resonance in medicine : official journal of the Society of Magnetic Resonance in Medicine / Society of Magnetic Resonance in Medicine. Aug 20.2012

[17]. Tropp J, Lupo JM, Chen A, Calderon P, McCune D, Grafendorfer T, et al. Multi-channel metabolic imaging, with SENSE reconstruction, of hyperpolarized [1-(13)C] pyruvate in a live rat at 3.0 tesla on a clinical MR scanner. Journal of magnetic resonance. Jan; 2011 208(1):171–7. [PubMed: 21130012]

[18]. Giovannetti G, Frijia F, Menichetti L, Milanesi M, Ardenkjaer-Larsen JH, De Marchi D, et al. Hyperpolarized 13C MRS surface coil: design and signal-to-noise ratio estimation. Medical physics. Oct; 2010 37(10):5361–9. [PubMed: 21089771]

[19]. Arunachalam A, Whitt D, Fish K, Giaquinto R, Piel J, Watkins R, et al. Accelerated spectroscopic imaging of hyperpolarized C-13 pyruvate using SENSE parallel imaging. Nmr Biomed. Oct; 2009 22(8):867–73. [PubMed: 19489035]

[20]. Glover GH, Hayes CE, Pelc NJ, Edelstein WA, Mueller OM, Hart HR, et al. Comparison of Linear and Circular-Polarization for Magnetic-Resonance Imaging. Journal of Magnetic Resonance. 1985; 64(2):255–70.

[21]. Tropp J. Image brightening in samples of high dielectric constant. Journal of Magnetic Resonance. Mar; 2004 167(1):12–24. [PubMed: 14987593]

[22]. Tropp J. Reciprocity and gyrotropism in magnetic resonance transduction. Phys Rev A. 2006:062103.

[23]. Harte PT, Smith TE, Williams JH, Degnan JR. Time series geophysical monitoring of permanganate injections and in situ chemical oxidation of PCE, OU1 area, Savage Superfund Site, Milford, NH, USA. J Contam Hydrol. May 1.2012 132:58–74. [PubMed: 22459605]

[24]. Reed G, von Morze C, Bok R, Koelsch B, Van Criekinge M, Smith K, et al. High Resolution C-13 MRI With Hyperpolarized Urea: Mapping and N-15 Labeling Effects. IEEE transactions on medical imaging. Oct 25.2013

[25]. Yen YF, Le Roux P, Mayer D, King R, Spielman D, Tropp J, et al. T-2 relaxation times of C-13 metabolites in a rat hepatocellular carcinoma model measured in vivo using C-13-MRS of hyperpolarized [1-C-13]pyruvate. Nmr Biomed. May; 2010 23(4):414–23. [PubMed: 20175135]

[26]. Hajipour AR, Adibi H, Ruoho AE. Wet silica-supported permanganate for the cleavage of semicarbazones and phenylhydrazones under solvent-free conditions. J Org Chem. May 30; 2003 68(11):4553–5. [PubMed: 12762769]

[27]. Ross C, Murdoch LC, Freedman DL, Siegrist RL. Characteristics of potassium permanganate encapsulated in polymer. J Environ Eng-Asce. Aug; 2005 131(8):1203–11.

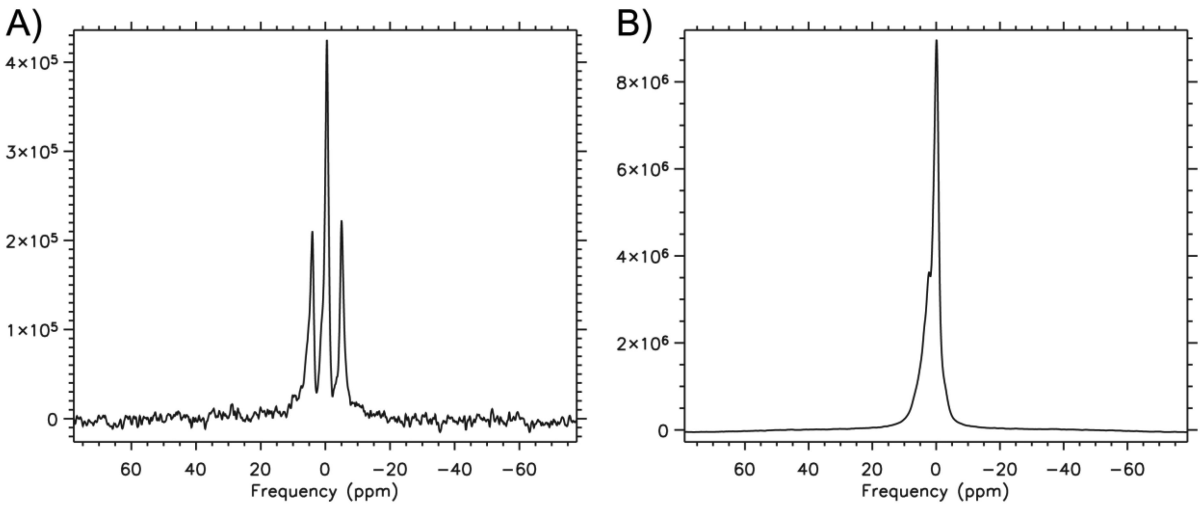

Figure 1.

Comparative 90° "pulse and acquire" NMR spectra (real component, phased) for two phantoms described in text, acquired in human head coil tuned for ^{13}C at 3T. Natural abundance ethylene glycol ^{13}C spectrum (A) and 3.0M aqueous $NaMnO_4$ ^{55}Mn spectrum (B), centered on their respective Larmor frequencies. Each spectrum was obtained in a single acquisition (no signal averaging).

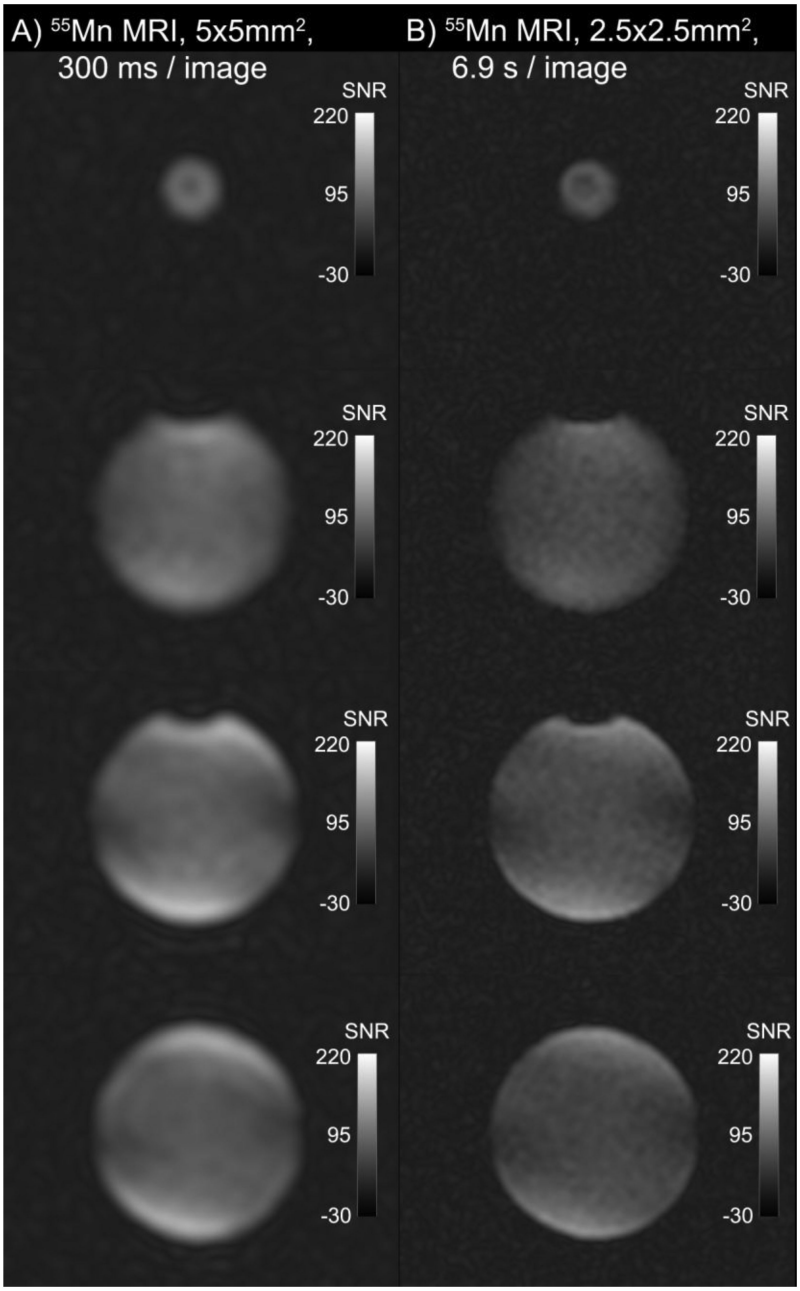

Figure 2.

Axial multi-slice bSSFP ^{55}Mn MRI images of 2.7M aqueous $NaMnO_4$ phantom at 3T, acquired in human ^{13}C head coil at two spatial resolutions, 5×5mm^2 (A) and 2.5×2.5mm^2 (B). Scale bars show the approximate image SNR.

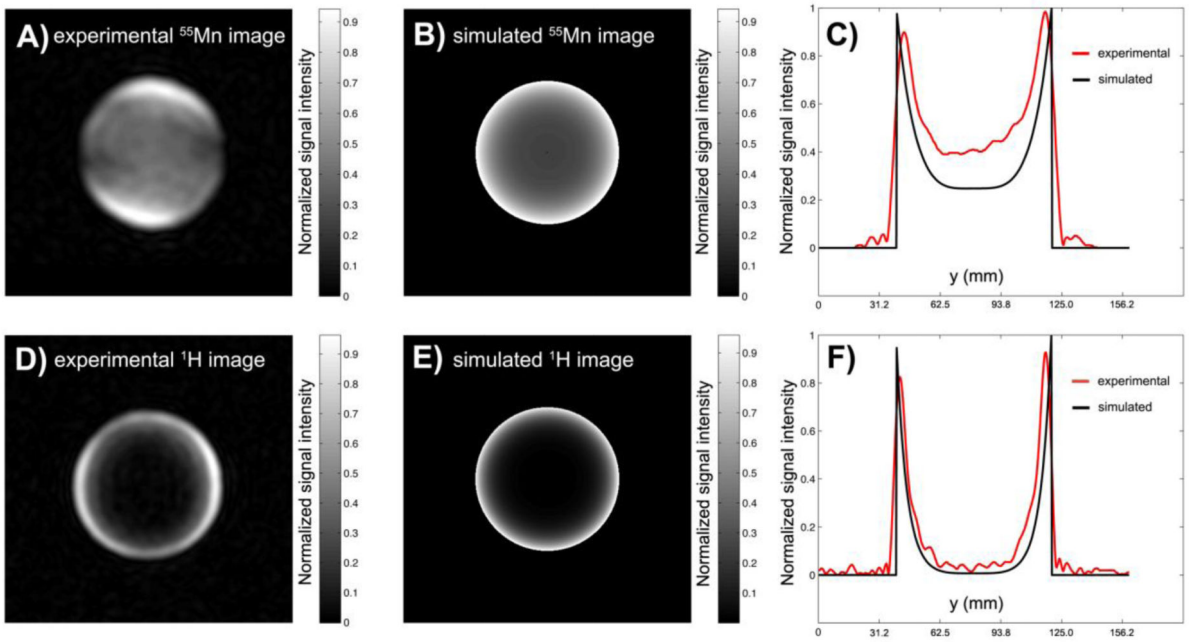

Figure 3.

Experimental and simulated multi-nuclear MRI images of 2.7M aqueous $NaMnO_4$ phantom at 3T. Experimental MRI images of ^{55}Mn (A) and ^{1}H (D), and corresponding simulated images of ^{55}Mn (B) and ^{1}H (E). Actual (red) and simulated (black) image signal profiles for ^{55}Mn (C) and ^{1}H (F).

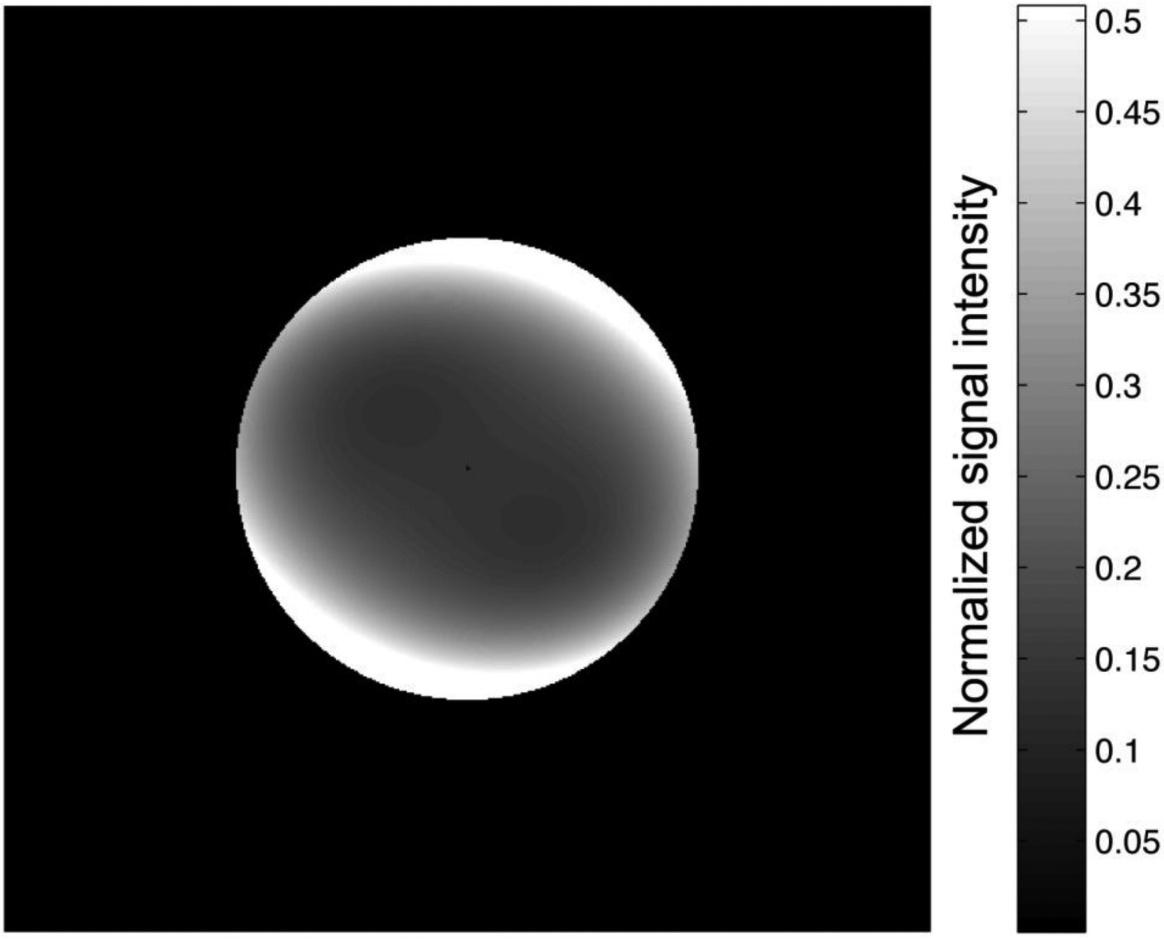

Figure 4.

Simulated ^{55}Mn MRI image including simulated artifact resulting from partial quadrature imbalance of the RF coil. The appearance of this image corresponds slightly more closely to the experimental image in Fig. 3A than the conventional simulation shown in Fig. 3B, potentially indicating a contribution from this effect to the appearance of the experimental ^{55}Mn MRI images.